ORGANIC RANKINE CYCLE PART-LOAD CHARACTERIZATION: VALIDATED MODELS OF AN 11 KWE WASTE HEAT RECOVERY ORC

Lecompte S.*[a], Ameel, B.[a], van den Broek M.[a], De Paepe M.[a]
*Author for correspondence
[a]Department of Flow, Heat and Combustion Mechanics
Ghent University,
Sint-Pietersnieuwstraat 41,
9000 Gent,
Belgium
E-mail: steven.lecompte@ugent.be

ABSTRACT

The organic Rankine cycle (ORC) is a mature technology for converting low temperature heat to electricity. However before large scale adoption in waste heat recovery applications is attained companies need to be convinced of the benefits. Considering the appraisal of an ORC project is mainly motivated by the financial gain, an accurate prediction of the power output is essential. Yet, when considering waste heat valorisation, the majority of applications have time varying waste heat streams. As such detailed models are necessary to account for part-load operation. This work aims to develop robust and computationally effective part-load models for ORCs. Important is that these models are thoroughly validated based on experimental results from a scaled down 11 kWe waste heat recovery ORC. Special attention has been paid in detecting stable experimental steady state data points for validation. The validated model presented is able to accurately predict the net power output within ±2%.

INTRODUCTION

In contrast to heat from most renewable sources, waste heat can have large variations in time of capacity and temperature. Examples of these capacity and temperature variations can amongst others be found in the cement industry (drying processes) [1], transportation sector (mobile combustion engines) [2] and steel industry (electric arc furnaces, cokes ovens) [3]. These variations make it difficult to assess the real power output of the organic Rankine cycle (ORC). Because the ORC operating point deviates from the nominal regime, part-load models are necessary.

In the research literature there is a specific focus on the part-load operation of ORCs. Gurgenci [4] analysed the part-load performance of ORCs for solar applications. Sun and Li [5] investigated the part load performance of ORCs for waste heat valorisation. Manente et al. [6] simulated the part load performance of a geothermal plant. Ibarra et al. [7] simulated a 5 kWe ORC at part-load operation. However all the above cited papers omit validating the modelling results with experimental data. Studies that combine part-load modelling with experimental validation are extremely scarce. Notable publications that provide validated part-load models for the subcritical ORC are these by Quoilin et al. [8] and Bracco et al. [9].

In the presented work, semi-empirical models of the individual components of the ORC are introduced. The models were chosen for an optimal balance between prediction capability, accuracy and computational time. These component models are afterwards interconnected to simulate the ORC based on the input conditions of pump and expander speed. Finally the full cycle model is validated on experimental data from an 11 kWe ORC.

NOMENCLATURE

A	[m²]	Heat exchange area
C	[-]	Dimensionless coefficient
h	[kJ/kg]	Enthalpy
T	[°C]	Temperature
$\dot{m}$	[kg/s]	Mass flow rate
N	[rpm]	Rotational speed
p	[bar]	Pressure
r_v	[-]	Volume ratio
$\dot{Q}$	[kW]	Heat flow rate
$\dot{V}$	[m³/h]	Volume flow rate
v	[m³/kg]	Specific volume
$\dot{W}$	[kW]	Power
Special characters		
ε	[-]	Isentropic efficiency
η_{loss}	[-]	Lumped loss coefficient
ψ	[-]	Filling factor

Subscripts	
cf	Cooling fluid
exp	Expander
hf	Hot fluid stream (i.e waste heat)
internal	Value internal expansion
wf	Working fluid

EXPERIMENTAL SET-UP

An 11 kWe organic Rankine cycle set-up is used for validating the part-load models. This experimental set-up is a scaled down version of a real commercial ORC designed for low heat source temperatures (between 80 °C and 150 °C) and uses R245fa as working fluid. The data capturing is done with a sample rate of 1 Hz. A schematic of the measurement equipment is given in Figure 1. A picture of the installation is given in Figure 2. In the presented tests, the recuperator is

bypassed in order to reduce modelling errors on the cycle. Because partial condensation appears in the recuperator it is not possible to have a closed heat balance, as such it is impossible to assess the heat losses without accurate measurement of the vapor fraction. The recuperator in this system is also not insulated. Furthermore, on a component level, the addition of the recuperator provides little additional information as the condenser and evaporator are geometrically completely identical.

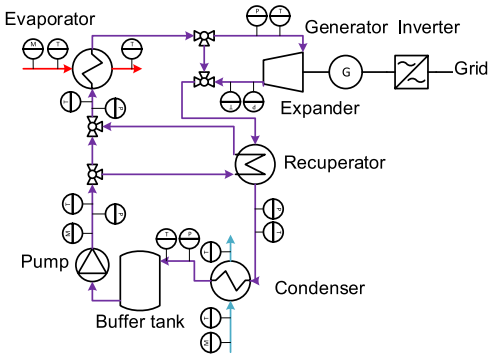

Figure 1 Schematic layout ORC set-up.

Figure 2: Photograph of the 11 kWe ORC set-up.

All of the heat exchangers (evaporator, condenser, recuperator) in the system are identical and of the brazed plate heat exchanger type. Geometric details about the heat exchangers are provided in Table 1. The evaporator is insulated with glass wool (thermal resistance value of 4.5 m²/K/W). The other heat exchangers are not insulated. There is a bypass installed over the recuperator to support measurements without recuperator. Tests reported in this work are done without recuperator. A centrifugal turbopump is chosen to pressurize the working fluid. The characteristics are found in Table 2. The expander is a volumetric double screw machine. Details about the expander are not disclosed. The heating loop consists of a Maxxtec® heater made up of 10 x 25 kWe electrical heaters. The maximum thermal oil flow is 14 m³/h at a maximum temperature of 340 °C. The thermal oil used is Therminol 66. The cooling loop consists of an air cooled condenser with a rated capacity of 480 kW at 20 °C ambient and respectively water input and output temperature of 70 °C and 90 °C. The cooling medium is a mixture of water and glycol, with 33 vol% glycol. The maximum rated temperature and mass flow rate are respectively 120 °C and 20 m³/h. Details about the measurement equipment can be found in Table 3.

Table 1 Details of the plate heat exchangers.

Characteristic	Value
Model (-)	SWEP B200T SC-M
Number of plates (-)	150
Dimensions (mm)	525 x 353.5 x 243
Temperature range (°C)	-196 - 225
Maximal pressures (bar)	45 at 135 °C and 36 at 225 °C
Material (-)	stainless steel
Weight (kg)	69.8

Table 2 Details of the pump.

Characteristic	Value
Model (-)	Calpeda MXV 25-214
Nominal speed (rpm)	2900
Nominal power (kWe)	2.2
Head range (m)	1-4.5
Number of stages (-)	14
Material (-)	stainless steel AISI 304

Table 3 Details of the measurement equipment.

Measure	Type	Equipment
$\dot{m}_{wf}$	Coriolis flow meter	E+H, Promass F
$\dot{m}_{hf}$	Pressure orifice	Rosemount 3051
$\dot{m}_{cf}$	Ultrasonic	Siemens Sitrans FUS 380
T_{wf}	RTD	E+H, TST487
T_{hf}	RTD	E+H, TR13
T_{cf}	RTD	E+H, TR90
p_{wf}	Absolute pressure sensor	WIKA A-10

MODELS

All of the models discussed in this section were implemented in MATLAB version 2015a [10]. Fluid properties came from the CoolProp library version 5.1.1 [11]. If calibration of the models is required, this is done with an extra dataset of 25 points gathered during the ORCNext [12] project during the period 24/08/2015 to 03/09/2015.

Heat exchangers

The implemented model of the heat exchanger is a hybrid approach between the finite volume models and the moving boundary models. In the moving boundary model, three zones are defined according to the state of the refrigerant: single phase liquid, two-phase liquid-vapour, single phase vapour. For a given geometry and inlet condition, the required heat exchange area for each zone is calculated. The outlet conditions follow from the equality of the calculated and the real heat exchange area in an iterative solving process ($A_{actual} = A_{zoneI} + A_{zoneII} + A_{zoneIII}$). The idea is that each zone can be adequately modelled with a set of lumped parameters. This

assumption has been proven valid for heat exchangers used in various systems. In the finite volume model, the heat exchange area is divided into a given number of equal volume parts. For each of these volumes the heat flow is calculated. Each volume consists of one zone; if there is a transition in the volume this introduces an error. The finite volume steady state modelling approach is not frequently used. However if enough segments (N≈15) are used good results can be achieved. When modelling supercritical heat exchangers, the assumption of a single supercritical zone would lead to large discrepancies. In this instance the finite volume steady-state model is required [13, 14]. However experimental validations under supercritical conditions are, according to the authors' knowledge, not available in public literature.

In Figure 3 the flow diagram of the hybrid solver is given. Initially the heat exchanger is discretised in N segments. These segments are interconnected according to the geometry of the heat exchangers. The P-NTU [15] correlations are used to determine the heat transfer in each segment. If there is a phase transition an additional segment is inserted. The lengths of the transition segments are calculated and the solver continues with calculating the heat transfer for the next segment. The calculation stops if all segments are handled. If N=0 the model is equal to a moving boundary model. The convective heat transfer correlations for plate heat exchanger are taken from: Martin [16] (single-phase), Han et al. [17] (two-phase evaporation) and Han et al. [18] (two-phase condensation).

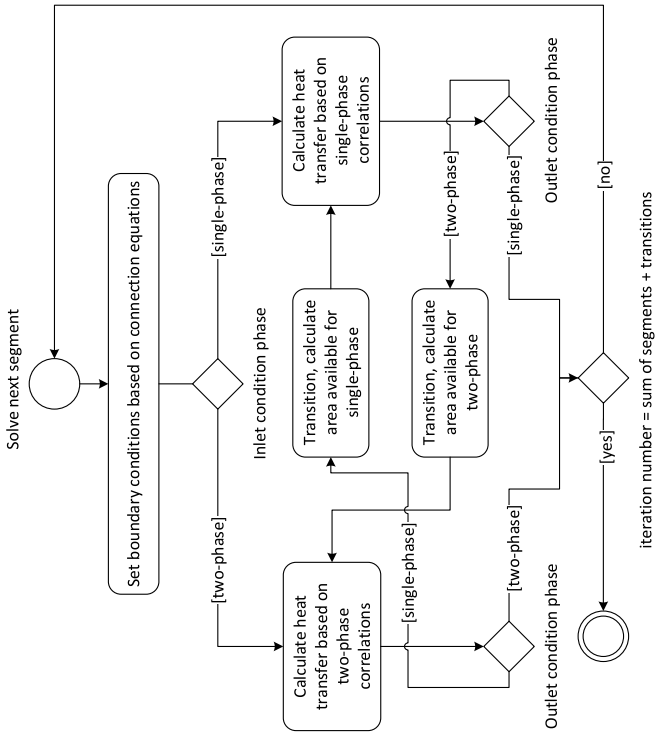

Figure 3: Flowchart solver hybrid finite-volume/moving boundary model.

Centrifugal pump

The centrifugal pump is typically described by characteristic curves. These depict the behaviour of head (i.e. pressure), power consumption and efficiency as function of the volume flow rate. For a fixed pumping speed there is a single curve relating the head with the volume flow rate and a second curve relating the efficiency with the volume flow rate. This data is shared by the manufacturer under normalized testing conditions [19]. The dimensionless curve is given in Figure 4. The dimensionless parameters are given in Eq. 1 and Eq. 2. A similar modelling approach, that uses dimensionless curves to model centrifugal pumps in ORC systems, is seen in the work of Manente et al. [6].

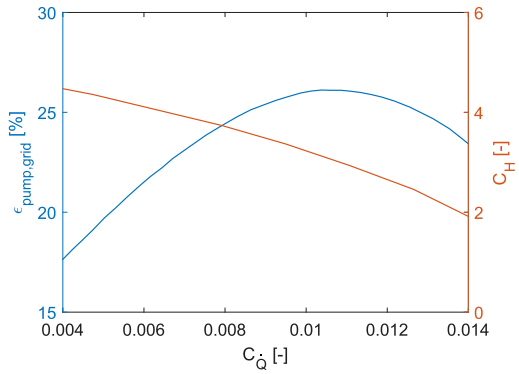

Figure 4: Dimensionless characteristic curve centrifugal pump.

$$C_{\dot{Q}} = \frac{\dot{Q}}{ND^3} \tag{1}$$

$$C_H = \frac{gH}{N^2 D^2} \tag{2}$$

Volumetric expander

A model for the volumetric expander inherently has two degrees of freedom. One related to the volumetric performance the other to the work output. The volumetric performance is calculated from the inlet and outlet boundary conditions by the equation forming the filling factor:

$$\psi = \frac{\dot{m}_{wf} v_{\exp,in}}{V_{\exp,\text{int}ernal} N_{\exp}} \tag{3}$$

The filling factor is modelled by introducing non-dimensional working conditions as given by Declaye et al. [20]:

$$r_p^* = \frac{r_p - 4}{4} \tag{4}$$

$$p^* = \frac{p_{\exp,in} - 10}{10} \tag{5}$$

$$\psi = a_1 + a_2 \ln\left(\frac{N_{\exp}}{5000}\right) + a_3 r_p^* + a_4 p^* \tag{6}$$

In these equations, r_p is the pressure ratio over the expander, $N_{\exp}$ the rotational speed of the expander and $p_{\exp,in}$ the inlet pressure of the expander. The values of a_1, a_2, a_3,

a_4 are fitted to calibration data: $a_1 = 1.0632$, $a_2 = 0$, $a_3 = 0.0438$, $a_4 = 0.0438$.

The isentropic efficiency relates the available energy of an adiabatic reversible process to the actual work output. In experimental works several definitions circulate, thus care should be taken. For example, the electricity output at the grid can be used, resulting in Eq. 7. Another option, Eq. 8, is to use the energy difference of the working fluid over the expander. Be aware that ambient losses are included in the definition of Eq. 6, these are not separated.

$$\varepsilon_{\exp,grid} = \frac{\dot{W}_{\exp,grid}}{\dot{W}_{\exp,isentropic}} \quad (7)$$

$$\varepsilon_{\exp,cycle} = \frac{\dot{m}_{wf}(h_{\exp,in} - h_{\exp,out})}{\dot{W}_{\exp,isentropic}} \quad (8)$$

$$\dot{W}_{\exp,isentropic} = \dot{m}_{wf}(h_{\exp,in} - h_{\exp,out,isentropic}) \quad (9)$$

The model for the isentropic efficiency is adapted from Lemort et al. [21]. Both $\varepsilon_{\exp,cycle}$ and $\varepsilon_{\exp,grid}$ are predicted from a model which includes two parameters: the internal built in volume ratio r_v and a lumped thermo-mechanical loss coefficient η_{loss}. The internal built in volume, r_v, is the ratio of specific volume at the outlet on the specific volume at the inlet of the expander. The expansion model is split into an isentropic expansion $(h_{\exp,in} - h_{\exp,\mathrm{int}ernal})$ and a constant volume expansion $((p_{\exp,\mathrm{int}ernal} - p_{\exp,out})r_v v_{\mathrm{nt}ernal})$, with $v_{i\,\mathrm{nt}ernal}$ the specific volume at the end of the isentropic expansion. The isentropic expansion fraction corresponds to a volume ratio increase r_v. The constant volume expansion fraction accounts for the expansion (or recompression) to the final discharge pressure. As such the following correlations are obtained:

$$\varepsilon_{\exp,grid} = \eta_{loss,\exp,cycle}\dot{m}_{wf}[(h_{\exp,in} - h_{\exp,\mathrm{int}ernal}) + (p_{\exp,\mathrm{int}ernal} - p_{\exp,out})r_{v,grid}v_{\mathrm{int}ernal}]$$

$$\varepsilon_{\exp,cycle} = \eta_{loss,\exp,cycle}\dot{m}_{wf}[(h_{\exp,in} - h_{\exp,\mathrm{int}ernal}) + (p_{\exp,\mathrm{int}ernal} - p_{\exp,out})r_{v,cycle}v_{\mathrm{int}ernal}]$$

In these equations, the coefficients r_v and η_{loss} are determined by least squares model fitting: $r_{v,grid} = 5.567$, $r_{v,cycle} = 4.495$, $\eta_{loss,\exp,grid} = 0.5148$, $\eta_{loss,\exp,cycle} = 0.6131$.

STEADY STATE DETECTION

The first step in pre-processing the data is finding the steady-state points of operation. The strict meaning of steady state means that for a property K of a system the partial derivative with respect to time is zero ($\frac{\partial K}{\partial t} = 0$). In experimental data reduction this constraint is relaxed and a deviation during a time window is accepted. Due to measurement errors and uncertainties, the strict definition of steady state is thus impractical to use. As such several approaches were formulated in literature. For example Woodland et al. [22] proposed a standard for an ORC steady state measurement detection. Measurements are made at 1 Hz intervals. These values are averaged over 30 consecutive recordings. This average is afterwards compared to averaged measurements taken 10 minutes later. The percentage change is then computed and compared to a predefined threshold. These thresholds can be found in Table 4. Other methods which make use of a time window are based on F-tests [23], t-tests [24], hotelling T^2 tests [25] etc. Also wavelet transforms [26] are used, where the choice of the characteristic scale substitutes the role of the time window.

Table 4: Steady state criteria used by Woodland et al [22].

Measurement	Steady state criteria
Temperature	Difference < 0.5 K
Pressure	Change < 2%
Mass flow rate	Change < 2%
Speed rotating equipment	Change < 2%

The steady state algorithm used in his work is derived from the work by Kim et al. [27]. Their algorithm was applied on experimental data of a residential air conditioner. This algorithm is widely applicable and is applied on data coming from various thermodynamic cycles. They furthermore conclude that the evaporator superheat and condenser subcooling are sufficient for determining the onset of steady state. Also according to Gusev et al. [28] the time required for the temperatures in the condenser to stabilize is longer than for all others in the ORC system under consideration. However in determining the steady state points of the system it is not sufficient to look anly at the condenser side. For example, consider the system is in steady state operation. When the setpoint of the turbine rotational speed changes abruptly, it will take some time before the effect will be felt in the condenser. This however does not mean the system is in steady state operation.

The procedure for finding the steady states points is outlined below:

- Identify a representative steady state zone. A representative steady state zone is identified after approximately one hour of operation. When the samples are taken, they should comply to the criteria of woodland et al. [1], else a subsequent time window is used.
- Calculate the reference standard deviations based on 600 samples. This standard deviation multiplied with 2 is used as the threshold. A reference standard deviation multiplied with 3 will remove less than 1% of the steady-state data assuming that the steady-state measurements are random and normally distributed [6].
- Calculate the forward moving window standard deviation over the data set. For the forward moving standard deviation σ_k, k is the number of the calculation window.

- Identify the steady state zones, these have a moving window standard deviation which is lower than the identified threshold.
- Take the average of the identified data points in the steady state zones.

Acquiring steady state points

The goal of these experiments is to have validation data points over a large operating range, the initial sampling plan includes two levels of heat source mass flow rate (1.5 and 3 kg/s), two levels of cold water volume flow rate (7 and 13.4 m³/h) and two heat source temperature levels (110 and 120 °C). The expander speed is fixed at 5000 rpm. In Figure 5 these input parameters and the electrical power delivered to the grid by the expander from the full dataset is shown.

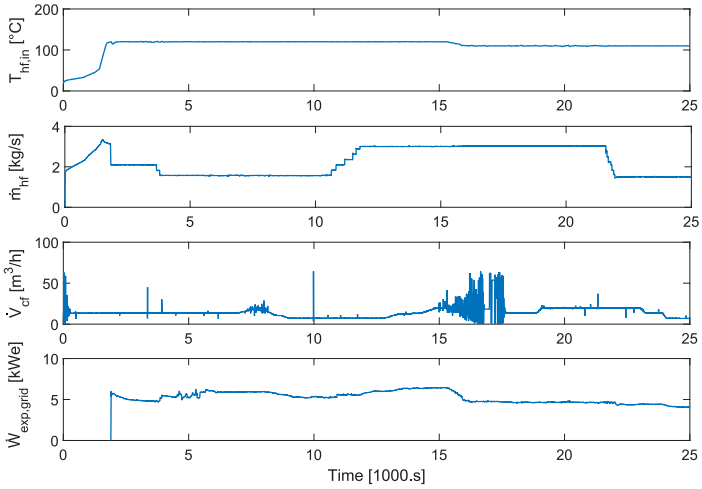

Figure 5 Original dataset of the performed ORC experiments, plot of $T_{hf,in}$, $\dot{m}_{hf}$, $\dot{V}_{cf}$ and $\dot{W}_{exp,grid}$.

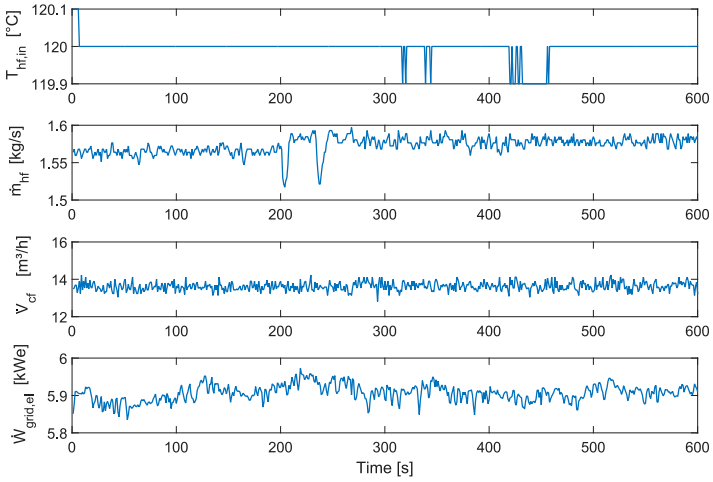

Figure 6 Reference steady state operating regime, plot of $T_{hf,in}$, $\dot{m}_{hf}$, $\dot{V}_{cf}$ and $\dot{W}_{exp,grid}$.

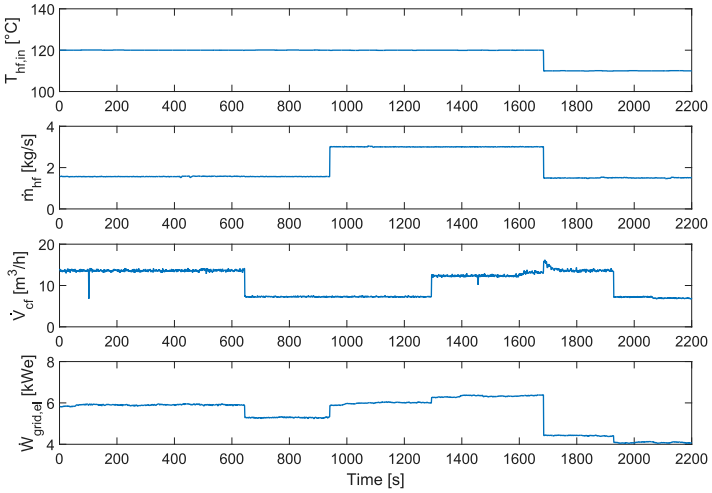

Figure 7 Detected steady state operating points, plot of $T_{hf,in}$, $\dot{m}_{hf}$, $\dot{V}_{cf}$ and $\dot{W}_{exp,grid}$.

As indicators for steady state operation are taken: the speed of the rotating equipment, the mass flow rate and inlet temperature of the heat source, the inlet and outlet pressure of the expander, the working fluid outlet temperature of the condenser, the volume flow rate of the cooling fluid and the working fluid inlet temperature at the expander. After an initial startup period of one hour the steady state reference values are acquired, these are shown in Figure 6. A time window of 10 minutes is used when calculating the moving window standard deviation. The resulting steady zones are shown in Figure 7 and the achieved operating ranges are given in Table 5.

Table 5 Range of achieved operating conditions of the steady-state cycle validation dataset.

Variable	Min. value	Max. value
$\dot{m}_{hf}$ (kg/s)	1.495	3.006
$\dot{V}_{cf}$ (m³/h)	7.038	14.465
$T_{hf,in}$ (°C)	110.0	120.0
$T_{hf,out}$ (°C)	83.0	103.4
$T_{exp,in}$ (°C)	107.8	119.5
$T_{exp,out}$ (°C)	78.3	88.0
$T_{superheat}$ (°C)	19.8	21.1
$p_{exp,in}$ (bar)	9.510	12.457
$p_{exp,out}$ (bar)	2.148	2.771
N_{pump} (rpm)	1973	2340
$\dot{m}_{wf}$ (kg/s)	0.2902	0.3874

VALIDATION RESULTS

Heat exchanger heat balances

In Figure 8 and Figure 9 the parity plot between the heat flow rate of the primary and secondary fluid side is shown respectively for the evaporator and the condenser. The uncertainty flags are calculated for both the secondary and primary fluid side. All of the points fall in a range of ±5% deviation relative to the parity line.

For the evaporator, the largest uncertainty is found on the hot fluid side. This is due to the large uncertainty on the mass flow rate measurement with the orifice flow meter. The uncertainties on the secondary and primary heat flow rate combined almost always include the parity line. This means that with the current measurement equipment it is impossible to discriminate further between ambient losses or the measurement uncertainties. For the condenser, the largest uncertainty is also found on the cold fluid side. This is again due to the lower accuracy of the mass flow rate measurement at the secondary side. As such the same remarks apply here. In contrast to the evaporator, the condenser is not insulated. However, the results are acceptable due to the lower temperature difference between the ambient conditions and the primary and secondary fluid.

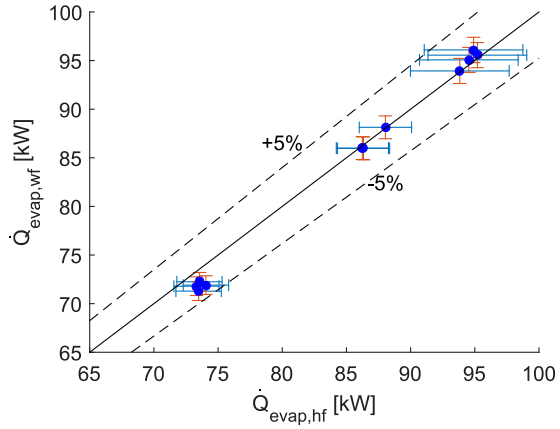

Figure 8 Heat balance over the evaporator with uncertainty flags.

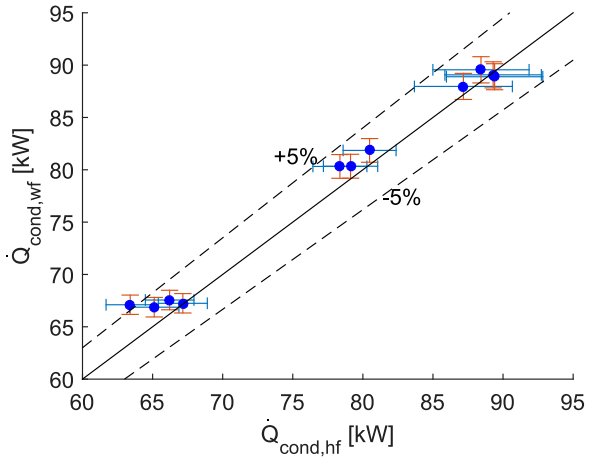

Figure 9 Heat balance over the condenser with uncertainty flags.

Results of the cycle model

The individual component models are interconnected to form the full cycle model, bypassing the recuperator. The only independent parameters to the cycle model are the pump speed and the expander speed. The prevailing dependent cycle parameters are the evaporating pressure, the condensing pressure and the working fluid mass flow rate. These internal parameters are influential in determining the net power output of the ORC.

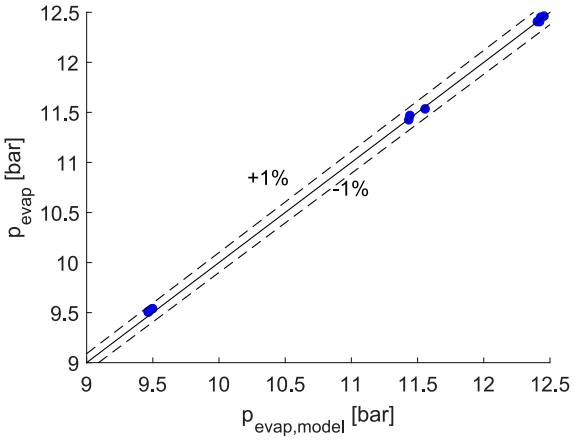

Figure 10 Parity plot of evaporation pressure, comparison between model and experiment.

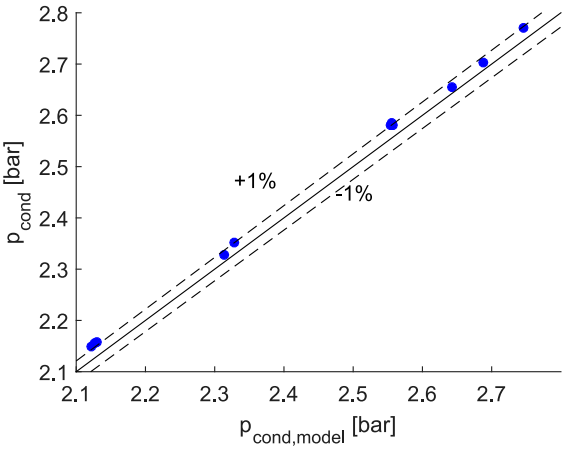

Figure 11 Parity plot of condensation pressure, comparison between model and experiment.

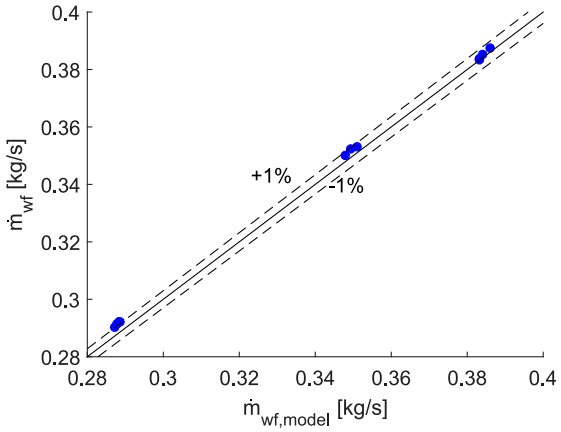

Figure 12 Parity plot of mass flow rate, comparison between model and experiment.

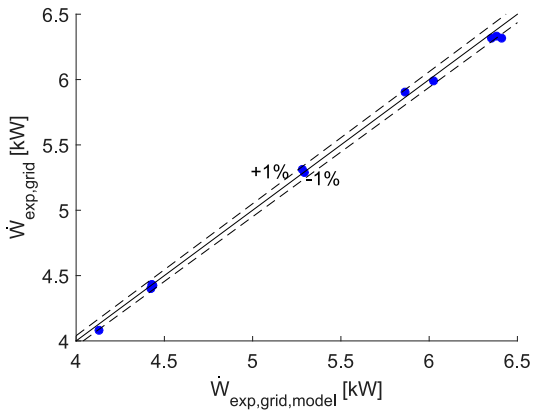

Figure 13 Parity plot of expander grid power output, comparison between model and experiment.

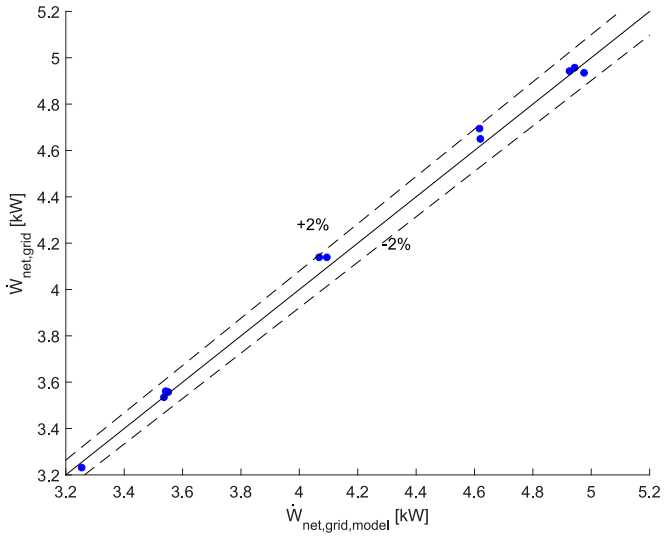

Figure 14 Parity plot of net power output, comparison between model and experiment.

First the parity plot of the evaporation pressure is given in Figure 10. A good match is seen between the resulting modelled pressure and the pressure measured before the expander. All of the points deviate less then ±1% from the experimental value. The parity plot for the condensing pressure is shown in Figure 11. In this case the resulting pressure from the model is compared with the measured pressure after the expander. Again a good match can be seen, with most of the modelled data points having a deviation less than ±1% compared to the measured pressure. The mass flow rate parity plot is given in Figure 12. Most of the modelled mass flow rates here have a deviation less than ±1% with the measured mass flow rate. Thus, based on the important internal parameters pressure and mass flow rate, the modelled ORC gave satisfactory results. Finally the modelled versus measured electrical expander power output and net power output is depicted in respectively Figure 13 and Figure 14. The net power output can be considered the single most important parameter and this value is typically predicted within ±2% of the measured value. The time to calculate a single point is approximately 3 seconds on a single Intel Xeon E5-2640 v3 core. In general, these are satisfactory result that gives confidence in using these models in further part-load analysis.

CONCLUSION

In this paper, experimental steady state data was gathered on a scaled down version of a commercial 11 kWe ORC. An important aspect in the data processing is the detecting of the steady state regions. Because of deviations in the measured data, due to the finite accuracy of the sensors and measuring equipment, the strict definition of steady state operation is not practical. As such a statistical detection algorithm was proposed based on the calculation of the moving window deviation.

Semi-empirical models from literature were carefully selected based on their predictive power and computational efficiency. The models were afterwards validated on an experimental dataset. Most of the heat flow rates of the condenser and evaporator are predicted within ±2% of the measured value. The mass flow rates at the expander are predicted within approximately ±1%, for the pump this is ±2%. The electrical power output of the expander is predicted within ±2%. The pump electrical power input is predicted within ±5%. Considering the relative low pumping power compared to the expander power this is not detrimental in determining the net power output. Finally, the validation results of the interconnected cycle model were presented. The important dependent parameters are the evaporation pressure p_{evap}, the condensation pressure p_{cond} and the working fluid mass flow rate $\dot{m}_{wf}$. All three predicted parameters show a maximum deviation of less than ±1% from the measured value. The modelled net power output deviates less than ±2% from the measured value. In future work, these models will be used to determine the optimal operating regime and to simulate the ORC under time-varying waste heat input.

ACKNOWLEDGEMENT

The results presented in this paper have been obtained within the frame of the IWT SBO-110006 project The Next Generation Organic Rankine Cycles (www.orcnext.be), funded by the Institute for the Promotion and Innovation by Science and Technology in Flanders. This financial support is gratefully acknowledged.

REFERENCES

[1] H. Legmann. Recovery of industrial heat in the cement industry by means of the ORC process. 2002. pp. 29-35.
[2] T.A. Horst, H.-S. Rottengruber, M. Seifert, J. Ringler. Dynamic heat exchanger model for performance prediction and control system design of automotive waste heat recovery systems. Applied Energy. 105 (2013) 293 - 303.
[3] G. David, F. Michel, L. Sanchez. Waste heat recovery projects using Organic Rankine Cycle technology: Examples of biogas engines and steel mills applications. 2011.
[4] H. Gurgenci. Performance of power plants with organic Rankine cycles under part-load and off-design conditions. Solar Energy. 36 (1986) 45-51.

[5] J. Sun, W. Li. Operation optimization of an organic rankine cycle (ORC) heat recovery power plant. Applied Thermal Engineering. 31 (2011) 2032-41.
[6] G. Manente, A. Toffolo, A. Lazzaretto, M. Paci. An Organic Rankine Cycle off-design model for the search of the optimal control strategy. Energy. 58 (2013) 97 - 106.
[7] M. Ibarra, A. Rovira, D.-C. Alarcón-Padilla, J. Blanco. Performance of a 5 kWe Organic Rankine Cycle at part-load operation. Applied Energy. 120 (2014) 147-58.
[8] S. Quoilin, V. Lemort, J. Lebrun. Experimental study and modeling of an Organic Rankine Cycle using scroll expander. Applied Energy. 87 (2010) 1260 - 8.
[9] R. Bracco, S. Clemente, D. Micheli, M. Reini. Experimental tests and modelization of a domestic-scale ORC (Organic Rankine Cycle). Energy. 58 (2013) 107-16.
[10] I. The MathWorks. MATLAB Release 2015a. Natick, Massachusetts, United States., 2015.
[11] I.H. Bell, J. Wronski, S. Quoilin, V. Lemort. Pure and Pseudo-pure Fluid Thermophysical Property Evaluation and the Open-Source Thermophysical Property Library CoolProp. Industrial & Engineering Chemistry Research. 53 (2014) 2498-508.
[12] M. De Paepe. Situation of the ORCNext project. 2012.
[13] S. Karellas, A. Schuster, A.-D. Leontaritis. Influence of supercritical ORC} parameters on plate heat exchanger design. Applied Thermal Engineering. 33–34 (2012) 70 - 6.
[14] S. Lecompte, S. Lemmens, H. Huisseune, M. van den Broek, M. De Paepe. Multi-Objective Thermo-Economic Optimization Strategy for ORCs Applied to Subcritical and Transcritical Cycles for Waste Heat Recovery. Energies. 8 (2015) 2714.
[15] R.K. Shah, D.P. Sekulic. Fundamentals of Heat Exchanger Design. Wiley2003.
[16] H. Martin. VDI Heat Atlas. 2010.
[17] D.-H. Han, K.-J. Lee, Y.-H. Kim. Experiments on the characteristics of evaporation of R410A in brazed plate heat exchangers with different geometric configurations. Applied Thermal Engineering. 23 (2003) 1209-25.
[18] D. Han, K. Lee, Y. Kim. The characteristics of condensation in brazed plate heat and exchangers with different chevron angles. Journal of the Korean Physical Society. 43 (2003) 66-73.
[19] Implementing Directive 2009/125/EC of the European Parliament and of the Council with regard to ecodesign requirements for water pumps.
[20] S. Declaye, S. Quoilin, L. Guillaume, V. Lemort. Experimental study on an open-drive scroll expander integrated into an ORC} (Organic Rankine Cycle) system with R245fa} as working fluid. Energy. 55 (2013) 173-83.
[21] V. Lemort, S. Quoilin, C. Cuevas, J. Lebrun. Testing and modeling a scroll expander integrated into an Organic Rankine Cycle. Applied Thermal Engineering. 29 (2009) 3094 - 102.
[22] B.J. Woodland, J.E. Braun, G. E.A., W.T. Horton. Experimental Testing of an Organic Rankine Cycle with Scroll-type Expander. 2012.
[23] S. Cao, R.R. Rhinehart. An efficient method for on-line identification of steady state. Journal of Process Control. 5 (1995) 363-74.
[24] B. Onoz, M. Bayazit. The power of statistical tests for trend detection. Turkish Journal of Engineering and Environmental Sciences. 27 (2003) 247-51.
[25] S. Narasimhan, C.S. Kao, R.S.H. Mah. Detecting changes of steady states using the mathematical theory of evidence. AIChE Journal. 33 (1987) 1930-2.
[26] T. Jiang, B. Chen, X. He, P. Stuart. Application of steady-state detection method based on wavelet transform. Computers \& Chemical Engineering. 27 (2003) 569-78.
[27] M. Kim, S.H. Yoon, P.A. Domanski, W.V. Payne. Design of a steady-state detector for fault detection and diagnosis of a residential air conditioner. International Journal of Refrigeration. 31 (2008) 790-9.
[28] S. Gusev, D. Ziviani, I. Bell, M. De Paepe, M. van den Broek. Experimental comparison of working fluids for organic rankine cycle with single-screw expander. 15th International Refrigeration and Air Conditioning Conference at Purdue, Proceedings. Purdue Univerisity2014. pp. 1-10.